Quantum plasmons with optical-range frequencies in doped few-layer graphene

Sharmila N. Shirodkar,[1,*] Marios Mattheakis,[1,2] Paul Cazeaux,[3,†] Prineha Narang,[1,4] Marin Soljačić,[5] and Efthimios Kaxiras[1]

[1]*John A. Paulson School of Engineering and Applied Sciences, Harvard University, Cambridge, Massachusetts 02138, USA*

[2]*Department of Physics, University of Crete, P.O. Box 2208, 71003 Heraklion, Greece*

[3]*School of Mathematics, University of Minnesota, Minneapolis, Minnesota 55455, USA*

[4]*Faculty of Arts and Sciences, Harvard University, Cambridge, Massachusetts 02138, USA*

[5]*Department of Physics, Massachusetts Institute of Technology, 77 Massachusetts Avenue, Cambridge, Massachusetts 02139, USA*

(Received 17 December 2017; revised manuscript received 18 March 2018; published 21 May 2018)

Although plasmon modes exist in doped graphene, the limited range of doping achieved by gating restricts the plasmon frequencies to a range that does not include the visible and infrared. Here we show, through the use of first-principles calculations, that the high levels of doping achieved by lithium intercalation in bilayer and trilayer graphene shift the plasmon frequencies into the visible range. To obtain physically meaningful results, we introduce a correction of the effect of plasmon interaction across the vacuum separating periodic images of the doped graphene layers, consisting of transparent boundary conditions in the direction perpendicular to the layers; this represents a significant improvement over the exact Coulomb cutoff technique employed in earlier works. The resulting plasmon modes are due to local field effects and the nonlocal response of the material to external electromagnetic fields, requiring a fully quantum mechanical treatment. We describe the features of these quantum plasmons, including the dispersion relation, losses, and field localization. Our findings point to a strategy for fine-tuning the plasmon frequencies in graphene and other two-dimensional materials.

DOI: 10.1103/PhysRevB.97.195435

I. INTRODUCTION

Collective excitations of electrons in metals, generically referred to as plasmons, have been attracting new attention recently in the realm of nanoparticles and low-dimensional materials. In these systems, new plasmonic phenomena continue to be discovered, beyond what was observed in conventional crystalline solids. These phenomena include quantum interference of plasmons, observation of quantum coupling of plasmons to single-particle excitations, and quantum confinement of plasmons in nanometer-scale particles and materials. These phenomena, intriguing in their own right, are also important for multifaceted applications. Plasmonic nanostructures are finding applications in integrated nanophotonics [1], biosensing [2–4], photovoltaic devices [5–7], single-photon transistors [8], single-molecule spectroscopy [9], and metamaterials [10,11]. The current interest in quantum nanophotonics and plasmonics is in part, driven by new materials, particularly low-dimensional solids, that access new ranges of frequency and transmission speeds. The reduced dimensionality of plasmons in two-dimensional (2D) materials provides ultrasubwavelength confinement with phase velocities several orders of magnitude lower than the speed of light [12]. In the present work we show that by properly controlling the density of metallic electrons in few-layer graphene, the prototypical 2D metal, the plasmon frequency can be pushed into the visible to near-infrared range, a feature highly desirable for optoelectronic applications and heretofore unattainable.

Graphene is quite special for 2D plasmonics [13], exhibiting intriguing properties such as extremely high electrical mobility [14] and easily tunable electron- and hole-doping concentrations (n_e,n_h) through gating [14,15]. The plasmon frequencies in graphene are controlled through doping [13], where typical doping concentration values achieved by gating are $\approx 10^{11}$ cm^{-2}, and the heaviest doping reached [16] is $n_h > 10^{13}$ cm^{-2}. Plasmons in gate-doped graphene typically emerge in the infrared to terahertz ranges and seldom in the mid- or near-infrared range [4,16,17]. So far, reaching the visible range for 2D plasmons in graphene, a crucial requirement for optoelectronic applications, has remained elusive. Searching for materials beyond graphene to achieve plasmons with optical frequencies is a possible route. For example, one possibility is the family of 2D materials referred to as transition-metal dichalcogenides (TMDCs), but plasmons in these materials are predicted to appear at terahertz frequencies [18,19]. Another possible solution, the plasmon mode on Be(0001) [13] observed in the visible range [20], cannot be interpreted as a true 2D plasmon since it has finite penetration depth into the underlying bulk material. A recent report by Huang *et al.* [21] predicts that the triangular polymorph of a 2D boron sheet exhibits visible frequency plasmons. But freestanding triangular 2D boron is dynamically unstable [22], and its experimental synthesis is quite difficult, which makes it challenging for device applications.

We propose here an alternative approach for breaking the impasse by doping few-layer graphene structures to levels beyond what is achievable through gating. Although there have been previous reports of optical-frequency plasmons in graphene monolayers with adsorbed Li atoms (LiC_2) [23], this configuration is energetically unstable, as we have established in previous work [24], and therefore is unlikely to form

*Present address: Department of Materials Science and NanoEngineering, Rice University, Houston, Texas 77005, USA; sns8@rice.edu

†Present address: Department of Mathematics, University of Kansas, Lawrence, Kansas 66045, USA.

experimentally; encapsulating the Li atoms between graphene layers, as in the structures proposed and studied here, is required to stabilize the doped system. Experiments have proved the feasibility of inserting metal atoms like lithium (Li) between layers of 2D materials [25,26], resulting in heavy doping. Inspired by this, we use a theoretical approach based on first-principles electronic structure calculations to explore the possibility of observing quantum plasmons in the visible range for Li-intercalated two- and three-layer graphene. The origin of 2D plasmons is related to the local-field effects and the nonlocal response of the material to external fields [27]. Hence, the study of these waves demands a fully quantum mechanical description of the material properties, which compels us to call them "quantum" 2D plasmons. We effectively capture the quantum nature of these plasmons through our accurate, high-fidelity first-principles calculations, distinguished by (i) our methodology, which correctly confines plasmons in two dimensions, and (ii) a realistic estimate of carrier lifetime, a crucial factor that determines plasmon losses. Our results show that quantum plasmons in few-layer graphene are indeed feasible. This opens new pathways for fine-tuning a wide range of plasmon frequencies, including the visible range, in 2D structures by controlling the concentration and type of intercalants.

II. COMPUTATIONAL METHODS

Our first-principles calculations are based on density functional theory (DFT) as implemented in the GPAW package [28,29]. The interaction between ionic cores and valence electrons is described by the projector augmented-wave method [30,31]. A vacuum of 25 Å is included to minimize the interaction between periodic images along the direction perpendicular to the plane of the sheets (z direction). The Kohn-Sham wave functions are represented using a plane-wave basis with an energy cutoff of 340 eV, and the exchange correlation energy of electrons is described using the local-density-approximation functional. For the linear response calculations, which are used to estimate the dielectric functions [32], we sample the Brillouin zone with a $256 \times 256 \times 1$ grid of k points to include an accurate description of intraband transitions. For the dielectric response calculations we use a plane-wave energy cutoff of 30 eV. All the other parameters were converged to within 0.05 eV of the plasmon energies, using the methodology developed by Andersen *et al.* [18,33] for calculating the quantum plasmon modes.

The potential $\phi(\mathbf{r},\omega)$ and charge density $\rho(\mathbf{r},\omega)$ of the quantum plasmon modes are obtained as left and right eigenfunctions (which satisfy the Poisson equation) of the dielectric operator $\hat{\epsilon}(\omega)$, diagonalized in the plane-wave basis:

$$\hat{\epsilon}(\omega)\phi_n(\omega) = [\hat{1} - \hat{v}\,\hat{\chi}^0(\omega)]\phi_n(\omega) = \lambda_n(\omega)\phi_n(\omega), \quad (1)$$

where ω and $\mathbf{r}$ denote the frequency and in-plane spatial vector, respectively. Here $\hat{\epsilon}(\omega)$ is expressed in terms of the noninteracting linear response operator $\hat{\chi}^0(\omega)$ and the Coulomb interaction operator $\hat{v} = 1/|\mathbf{r} - \mathbf{r}'|$. The condition for observing a plasmon at frequency ω_p is $\mathrm{Re}[\lambda_n(\omega)] = 0$ or, equivalently, a peak in the loss function, $-\mathrm{Im}[\lambda_n(\omega)]/|\lambda_n(\omega)|^2$.

A key ingredient in obtaining the plasmon dispersion relations and losses is the carrier lifetime τ. To obtain reliable values of τ, we used DFT results for the energies and matrix elements of both electrons and phonons (see the Supplemental Material [34] and Ref. [35]). This takes into account the detailed electronic structure effects such as the response of electrons far from the Dirac point, as well as scattering against both acoustic and optical phonons, including umklapp and intervalley processes [35–38]. Doping, that is, a change in the position of the Fermi level E_F changes the value of τ, and hence calculations were carried out for several different values of E_F ranging from the neutral (undoped) value to 1.5 eV above it (see the Supplemental Material [34] for details of formulation and [35] for values of τ). Interestingly, our results show that the extremely large $\tau \approx 1$ ps for freestanding undoped graphene drops to ≈ 29 fs in doped graphene. For simplicity and computational efficiency, we use doped monolayer graphene to obtain the values of τ for positions of E_F that correspond to those of the Li-doped bilayer and trilayer graphene; this is a reasonable approximation because, at high doping concentrations we expect that the effects of interlayer electron-phonon and electron-electron coupling on τ in intercalated graphene will be rather small compared to the effects of changing the position of E_F, which is properly taken into account by the procedure described.

III. TRANSPARENT BOUNDARY CONDITIONS

The standard approach for eliminating spurious effects due to the finite size of the vacuum [39] is inadequate for plasmons with small in-plane wave vectors $\mathbf{q}$, and increasing the size of the vacuum region until these effects become negligibly small requires very expensive calculations. A significant methodological contribution of the present work is the formulation and implementation of transparent boundary conditions which overcome the drawbacks of the Coulomb cutoff method and offer a more accurate description of the quantum plasmon fields. Let z_- and z_+ be the bounds of the supercell (simulation box) along the z direction (vacuum region), with the (x,y) plane being periodic. We apply a one-dimensional Fourier transform in the z direction to obtain a real-space representation in this coordinate. The response operator under the random-phase approximation (RPA) then has the form

$$\hat{\chi}^0\phi(z,\mathbf{G}_{xy},\mathbf{q},\omega) = \int_{z_-}^{z_+} \sum_{\mathbf{G}'_{xy}} \chi^0_{\mathbf{G}_{xy},\mathbf{G}'_{xy}}(z,z',\mathbf{q},\omega)\phi(z',\mathbf{G}'_{xy},\mathbf{q},\omega)dz', \quad (2)$$

where $\mathbf{G}_{xy}$, $\mathbf{G}'_{xy}$ are vectors of the in-plane reciprocal lattice. For values of z,z' inside the supercell, $z_- < z,z' < z_+$, the kernel $\chi^0_{\mathbf{G}_{xy},\mathbf{G}'_{xy}}(z,z')$ is deduced from $\chi^0_{\mathbf{G},\mathbf{G}'}$ by Fourier transform. The kernel is extended with zero values for z or z' that lie in the vacuum region outside this cell. We observe that Eq. (1) can be reformulated as the generalized eigenvalue problem [34]:

$$\hat{\chi}^0\phi_n(z,\mathbf{G}_{xy},\mathbf{q},\omega) = \frac{1-\lambda_n}{4\pi}\left(|\mathbf{q}+\mathbf{G}_{xy}|^2 - \frac{\partial^2}{\partial z^2}\right)\phi_n(z,\mathbf{G}_{xy},\mathbf{q},\omega), \quad (3)$$

with the additional constraint that $|\phi_n| \to 0$ as $z \to \pm\infty$ so the problem is well posed. The left-hand side vanishes in the vacuum region, and Eq. (3) reduces to the one-dimensional

Poisson equation. For any nonzero value of $|\mathbf{q}+\mathbf{G}_{xy}|$, we thus obtain an explicit solution,

$$\phi_n(z,\mathbf{G}_{xy},\mathbf{q},\omega)=\phi_n(z_\pm,\mathbf{G}_{xy},\mathbf{q},\omega)e^{-|\mathbf{q}+\mathbf{G}_{xy}||z_\pm-z|}$$

for $z\leqslant z_-$ and $z\geqslant z_+$. The continuity of ϕ_n and its first derivative with respect to z leads to the transparent boundary conditions at $z=z_\pm$:

$$\frac{\partial\phi_n}{\partial z}(\mathbf{q},\mathbf{G}_{xy},z_\pm,\omega)=\mp|\mathbf{q}+\mathbf{G}_{xy}|\phi_n(\mathbf{q},\mathbf{G}_{xy},z_\pm,\omega), \quad (4)$$

which implies that the charge density and potential do not see the periodic boundary along the z direction for any value of $\mathbf{q}$ and hence decay to zero as $z\to\pm\infty$. The imposition of additional constraints generalizes the previous approaches [39,40], which makes the transparent boundary conditions an improvement over the former techniques. We solve numerically by finite differences the eigenvalue problem in Eq. (3) restricted to the finite band $z_-\leqslant z\leqslant z_+$, with the boundary conditions of Eq. (4) (see the Supplemental Material for details [34]).

IV. RESULTS AND DISCUSSION

We model Li-intercalated graphene (G) multilayers with an in-plane $\sqrt{3}\times\sqrt{3}$ multiple of the primitive unit cell of graphene, with the G/Li/G (bilayer) and G/Li/G/Li/G (trilayer) structures. There is one Li atom per unit cell between each pair of layers (see Fig. 1) [24,41]. For the trilayer, we consider the structure with the two Li atoms at the same hollow site but between two different pairs of graphene layers, as this is the stablest configuration [41]. Li intercalation makes AA stacking energetically more preferable [24], and hence, both bilayer and trilayer structures are inversion symmetric. The separation between the layers increases by 0.14 and 0.11 Å relative to its value in the AA stacked graphene bilayer (3.52 Å) for the bilayer and trilayer, respectively. Due to band folding in the $\sqrt{3}\times\sqrt{3}$ unit cell, the high-symmetry K point and hence the Dirac point of the primitive graphene cell fold onto the Γ point in the Brillouin zone (BZ) in our simulations (see Fig. 1). AA stacking preserves the sublattice symmetry

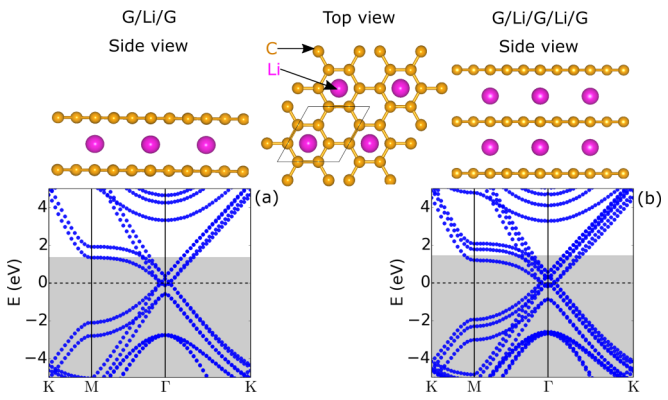

FIG. 1. Atomic structures (side and top views) and electronic structures of (a) the bilayer Li-intercalated graphene (G/Li/G) and (b) the trilayer Li-intercalated graphene (G/Li/G/Li/G). The shaded regions in (a) and (b) denote the occupied states, and the dashed black lines show the Dirac point/Fermi level in undoped layers.

of the layers and the linear dispersion of the electron bands at the Dirac point, unlike AB stacking, where the bands are parabolic [42]. Intercalation also leads to charge transfer from Li to the graphene layers and renders the system metallic (see Fig. 1) with $\approx 0.84e$ and $0.87e$ charge transferred from Li to bilayer and trilayer graphene (determined using Bader analysis), which corresponds to $n=5\times10^{14}$ cm^{-2} and $n=10^{15}$ cm^{-2}, respectively, subsequently shifting the Fermi level from the Dirac point into the conduction band by 1.35 eV and by 1.51 eV for the bilayer and trilayer, respectively, as seen in Fig. 1.

Since we consider metallic multilayers, more than one plasmon mode emerges [18,33,42]. Depending on the phase of the charge density and potential fields, we differentiate them as symmetric and antisymmetric plasmonic modes [see Figs. 2(a) and 2(d)]. For small $\mathbf{q}$, the decay length of 2D plasmons extends beyond the vacuum region, giving rise to interactions with periodic images and hence spurious fields and pseudocharges at the vacuum edge. On the other hand, our transparent boundary conditions correct these periodic interactions and make the plasmon tails invisible to one another for the same vacuum length. The charge density with (solid lines) and without (dotted lines) transparent boundary conditions is shown in Figs. 2(a) and 2(d) for G/Li/G and G/Li/G/Li/G, respectively. We also note that the charge transferred from Li is equally distributed in the unoccupied π^* orbitals, which is confirmed from the charge density distribution of the plasmon modes [see Figs. 2(a) and 2(d)], where the intensity of the fields is equal and reaches the maximum and minimum values away from the layers, consistent with the fact that the π^* orbitals of graphene extend away from the layers.

We plot the plasmon dispersion along Γ-M (the Γ-K direction is not as interesting in the band structure) with the magnitude of the real part of $\mathbf{q}$ ranging from $|\mathbf{q}|=q=0.007$ to 0.21 Å^{-1} since both plasmon modes become very weak above $q=0.21$ Å^{-1}. The symmetric mode is more dispersive than the antisymmetric mode and varies as $\sqrt{q}$ at small q, corresponding to a classical plasmon with Drude behavior due to intraband transitions. However, the antisymmetric mode varies almost linearly with q (has finite frequency at $q=0$) and relates to interband transitions between perfectly nested bands of the two layers [42]. In G/Li/G the plasmon frequencies are between 0.8 and 2.2 eV for $q\geqslant0.007$ Å^{-1}; the antisymmetric mode is in the optical frequency range even at low q, whereas the symmetric mode enters into this range at higher q values. The symmetric mode is always lower in energy than the antisymmetric mode due to finite coupling [42]. We note that the acoustic plasmon arising from the anisotropy of the bands crossing the Fermi level along Γ-M is not captured in our calculations due to limitations of the frequency grid, which is too coarse on the scale required to reveal this feature. However, this does not affect our conclusions since this particular mode is damped by the intraband transitions and therefore is not of interest here.

We quantify the plasmon losses from the ratio of real to imaginary components of the wave number, Re$[q]$/Im$[q]$ [43], which corresponds to the number of plasmon wavelengths that propagate before it loses most of its energy [see Fig. 2(c)]. For the doping in G/Li/G ($E_F=1.35$ eV), $\tau\approx29$ fs was calculated using our methodology discussed above, which is much shorter

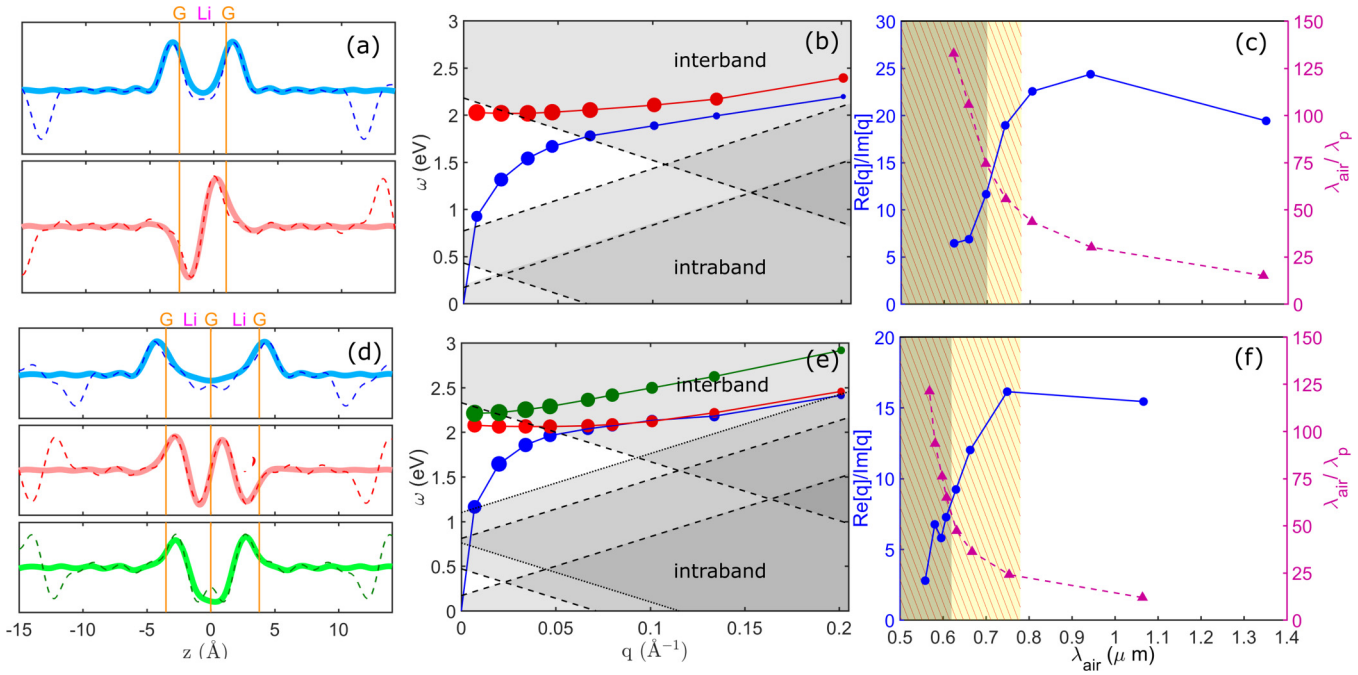

FIG. 2. Plasmon features for (a)–(c) the G/Li/G system and (d)–(f) the G/Li/G/Li/G system. (a) and (d) Plasmon charge density $\rho(\mathbf{r})$ at $q = 0.007$ Å^{-1} for the symmetric modes (blue and green lines) and the antisymmetric mode (red lines); solid lines (thicker and lighter shade) are for results with transparent boundary conditions, and dashed lines (thinner and darker shade) are for periodic boundary conditions with the Coulomb cutoff (see text). (b) and (e) Dispersion relation of plasmons along the Γ to M direction; the diameter of the circles is proportional to the strength of the resonance [18]. Shaded areas represent regions of inter- and intraband losses (including damping by optical phonons). (c) and (f) Re$[q]$/Im$[q]$ (left axis, solid blue line) and field localization (right axis, dashed magenta line), or "shrinkage," of the lowest symmetric mode. τ is ≈29 and 19 fs for the G/Li/G and G/Li/G/Li/G systems, respectively. The gray shaded areas denote the region of interband losses, and the yellow shaded (hatched) areas denote the visible frequency range, calculated with the Fermi velocity of graphene.

in comparison with $\tau \approx 135$ fs for $E_F = 0.135$ eV [43]. We give only the ratio for the symmetric (intraband) mode in Fig. 2(c). Due to its linear dispersion, the antisymmetric mode shows less variation in Re$[q]$/Im$[q]$ compared with the symmetric mode (see Fig. S1 in the Supplemental Material [34]). The in-plane propagation length of the plasmons varies directly with this ratio, with the symmetric plasmons propagating longer at longer wavelengths λ_{air}. We also calculate the wave "shrinkage," or the field localization of the plasmons, shown in Fig. 2(c); this corresponds to the ratio by which the plasmon wavelength λ_p is smaller than that in vacuum and is approximately 100 times for bilayer graphene.

There are three important decay modes that lead to plasmon damping: (i) Landau damping due to intraband losses when $\hbar\omega < \hbar v_F q$, (ii) interband losses (electron-hole transitions referred to as single-particle excitations (SPEs) identified as poles of the response function [42,44]) when $\hbar\omega > \hbar\omega_{SPE}$ (with the damping region defined by $\hbar\omega_{SPE} - \hbar v_F q < \hbar\omega < \hbar\omega_{SPE} + \hbar v_F q$), and (iii) decay through optical phonons in graphene for $\omega > \omega_{ph}$ ($\omega_{ph} = 0.2$ eV or 6.2 μm) [43] due to scattering of electrons (that is, plasmonic excitation) due to phonons. This calculation of the dielectric function under the RPA does not include the effects of electron-hole interactions, which are captured only by including a dynamically screened instead of bare Coulomb interaction. However, these excitons give rise to a prominent peak in the absorption spectrum near 4.5 eV [45], which is at a much higher energy than the visible frequency range. Also, doping has been shown to increase screening and reduce electron-hole interactions in graphene, leaving the optical response nearly identical to that of undoped graphene [45]. Hence, the exclusion of electron-hole interactions in our calculations does not affect the results.

In the case of G/Li/G, since the optical phonon $\omega_{ph} = 1400$ cm$^{-1} \equiv 0.17$ eV [41,46] is much smaller than the symmetric or antisymmetric plasmon frequencies (0.8 eV to 2.2 eV for $q \geqslant 0.007$ Å^{-1}), only multiple scatterings by phonons (which are less likely) will scatter plasmons into the damping regions. On the other hand, plasmons within the frequency range $\omega_{SPE} - \omega_{ph}$ to ω_{SPE} can get scattered by phonons into Landau/interband scattering regions, therefore making $\omega > \omega_{SPE} - \omega_{ph}$ the region where plasmons are damped by interband transitions and optical phonons. The SPEs at $q = 0$ were identified at 0, 0.6, and 2.4 eV, originating from the intraband, low-energy interband, and electron-hole interband transitions in G/Li/G. The damping regions are defined by $E_{SPE} \pm \hbar v_F q \pm \hbar\omega_{ph}$ (including scattering by optical phonons), where v_F is the Fermi velocity and E_{SPE} is the single-particle excitation energy [44,47] [see gray shaded areas in Fig. 2(b)]. Heavy doping by lithium pushes the electron-hole interband threshold for the bilayer to $\omega_{inter} \approx 1.77$ eV ($\lambda = 0.7$ μm). Since the optical frequency range ω_{op} is between 1.59 and 3.26 eV ($\lambda = 0.38$ to 0.78 μm) and $\omega_{inter} < \omega_{op}$, most of the symmetric and antisymmetric plasmon modes in this range are not damped by the interband transitions, indicated by the shaded regions in Figs. 2(b) and 2(e). Only for $q \geqslant 0.06$ Å^{-1} are the symmetric and antisymmetric modes damped.

To push the interband threshold frequency, and hence the plasmon frequencies, higher into the optical range (>2 eV), the Fermi level needs to be moved farther into the conduction bands. Since the maximum possible intercalation in bilayer graphene corresponds to the composition $C_{12}Li$, additional Li can be incorporated only by having more than two graphene layers. We therefore explore trilayer graphene since it can accommodate two Li layers, with the composition Li_2C_{18}, which increases the doping level to $E_F = 1.51$ eV. There are three modes in the trilayer structure in the 1.2–2.8 eV frequency range along the Γ-M direction for $q \geqslant 0.007$ Å^{-1}, two of which are symmetric and one of which is antisymmetric, as shown in Fig. 2(d). The third (second symmetric) mode emerges due to the third graphene layer, which brings in additional nesting of the bands. Similar to the bilayer case, the first symmetric mode due to intraband excitations exhibits $\sqrt{q}$ dependence, and the other two modes disperse linearly [see Fig. 2(e)]. The loss function shows larger variations in the peak positions for the first symmetric mode due to $\sqrt{q}$ behavior at low q compared to the antisymmetric mode (see Fig. S2 in the Supplemental Material for details [34]). More interestingly, the first symmetric and antisymmetric bands in the dispersion spectrum [red and blue curves in Fig. 2(e)] intersect, and the symmetric and antisymmetric modes are degenerate for $q > 0.067$ Å^{-1} along Γ-M. The reason behind this unusual degeneracy is the nesting between the bands at the Fermi level and, consequently, the absence of coupling between the two modes [42].

The higher doping concentration pushes the interband threshold frequency ω_{inter} to ≈ 2.0 eV (0.62 μm) for the first symmetric and antisymmetric modes in G/Li/G/Li/G. The poles at 0, 0.64, 0.93, and 2.5 eV correspond to the three damping regions associated with intraband, low-energy interband, and higher-energy electron-hole interband transitions. Hence, for 1.59 eV $< \omega <$ 2.0 eV (0.62 μm $< \lambda_{\text{air}} <$ 0.78 μm) the first symmetric and antisymmetric modes are undamped. More importantly, the second symmetric mode gets damped at a higher frequency ($\omega >$ 2.2 eV), so all three plasmon modes are undamped and emerge in the optical range for $q < 0.05$ Å^{-1}. The τ in graphene for such a high doping concentration ($E_F =$ 1.51 eV) is quite small, ≈ 19 fs (see the Supplemental Material [34]). From Re[q]/Im[q] in Fig. 2(f), we find that the first symmetric mode can be observed further into the mid-infrared range (from extrapolation; $\lambda_{\text{air}} > 3$ μm), whereas the other two modes have shorter wavelengths ($\lambda_{\text{air}} < 0.62$ μm). λ_p is also shrunk by approximately 100 times [Fig. 2(f)], as in the case of bilayer graphene, in agreement with previous reports [43]. We plot only the ratio for the first symmetric (intraband) mode in Fig. 2(f). Since the antisymmetric and second symmetric modes disperse linearly, the variation in Re[q]/Im[q] is small. These plasmons exhibit "shrinkage" similar to that of the symmetric mode (refer to Fig. S2 for further details [34]).

Controlling the number of layers and the concentration of intercalated Li atoms appears to be a feasible method for engineering the properties of visible plasmons for applications. For example, the mid-infrared-region plasmons in both the bilayer and trilayer Li-intercalated structures can be used for plasmonic biosensing [4,16]. We caution that certain technical aspects of the calculations reported here, like the choice of exchange-correlation functional for the electronic structure, can affect the electronic spectrum and can shift the plasmon energies to slightly different values than what we reported; such shifts could change the precise values of the damped plasmon frequencies, but we do not expect them to alter the overall picture. Damping due to the presence of defects and substrate phonons, features that were not included in the model of the physical system considered here, can also influence the existence of undamped 2D plasmons in the visible frequency range. A detailed analysis of these parameters will constitute the future scope of this work. Our work can be easily extended to explore other multilayers of other 2D materials (such as black phosphorus and transition-metal dichalcogenides) with different dopants and/or intercalants (K, Mg, Na etc.), opening up new pathways for fine-tuning the plasmon dispersion either by varying the number and type of layers and/or by varying the concentration and type of intercalant atoms.

ACKNOWLEDGMENTS

The authors thank R. Sundararaman and J. Joannopoulous for *ab initio* calculations and discussions related to plasmon lifetimes. The authors also thank J. Cheng, S. Inampudi, H. Mosallaei, and G. A. Tritsaris for useful discussions. M.M. acknowledges support from the EU program H2020-MSCA-RISE-2015-691209-NHQWAVE. We acknowledge support from ARO MURI Award No. W911NF14-0247 (S.N.S. and E.K.) and from EFRI 2-DARE NSF Grant No. 1542807 (M.M.). P.N. and M.S. were partly supported by the Army Research Office through the Institute for Soldier Nanotechnologies under Contract No. W911NF-13-D-0001. We used computational resources on the Odyssey cluster of the Research Computing Group at Harvard University and at the Extreme Science and Engineering Discovery Environment (XSEDE), which is supported by NSF Grant No. OAC-1053575.

[1] J. A. Schuller, E. S. Barnard, W. Cai, Y. C. Jun, J. S. White, and M. L. Brongersma, Nat. Mater. **9**, 193 (2010).
[2] F. Bender, P. Roach, A. Tsortos, G. Papadakis, M. I. Newton, G. McHale, and E. Gizeli, Meas. Sci. Technol. **20**, 124011 (2009).
[3] J.-M. Friedt, L. Francis, G. Reekmans, R. De Palma, A. Campitelli, and U. B. Sleytr, J. Appl. Phys. **95**, 1677 (2004).
[4] D. Rodrigo, O. Limaj, D. Janner, D. Etezadi, F. J. G. de Abajo, V. Pruneri, and H. Altug, Science **349**, 165 (2015).
[5] H. A. Atwater and A. Polman, Nat. Mater. **9**, 205 (2010).
[6] D. M. Schaadt, B. Feng, and E. T. Yu, Appl. Phys. Lett. **86**, 063106 (2005).
[7] C. Clavero, Nat. Photon. **8**, 95 (2014).
[8] D. E. Chang, A. S. Sørensen, E. A. Demler, and M. D. Lukin, Nat. Phys. **3**, 807 (2007).
[9] R. Zhang, Y. Zhang, Z. C. Dong, S. Jiang, C. Zhang, L. G. Chen, L. Zhang, Y. Liao, J. Aizpurua, Y. Luo, J. L. Yang, and J. G. Hou, Nature (London) **498**, 82 (2013).

[10] D. Liu, Y. Guo, L. Fang, and J. Robertson, Appl. Phys. Lett. **103**, 183113 (2013).
[11] M. Mattheakis, C. A. Valagiannopoulos, and E. Kaxiras, Phys. Rev. B **94**, 201404 (2016).
[12] W. F. Andress, H. Yoon, K. Y. M. Yeung, L. Qin, K. West, L. Pfeiffer, and D. Ham, Nano Lett. **12**, 2272 (2012).
[13] Z. Fei, A. S. Rodin, G. O. Andreev, W. Bao, A. S. McLeod, M. Wagner, L. M. Zhang, Z. Zhao, M. Thiemens, G. Dominguez, M. M. Fogler, A. H. C. Neto, C. N. Lau, F. Keilmann, and D. N. Basov, Nature (London) **487**, 82 (2012).
[14] K. S. Novoselov, A. K. Geim, S. V. Morozov, D. Jiang, Y. Zhang, S. V. Dubonos, I. V. Grigorieva, and A. A. Firsov, Science **306**, 666 (2004).
[15] A. Das, S. Pisana, B. Chakraborty, S. Piscanec, S. K. Saha, U. V. Waghmare, K. S. Novoselov, H. R. Krishnamurthy, A. K. Geim, A. C. Ferrari, and A. K. Sood, Nat. Nanotechnol. **3**, 210 (2008).
[16] H. Yan, T. Low, W. Zhu, Y. Wu, M. Freitag, X. Li, F. Guinea, P. Avouris, and F. Xia, Nat. Photon. **7**, 394 (2013).
[17] A. N. Grigorenko, M. Polini, and K. S. Novoselov, Nat. Photon. **6**, 749 (2012).
[18] K. Andersen and K. S. Thygesen, Phys. Rev. B **88**, 155128 (2013).
[19] K. Andersen, S. Latini, and K. S. Thygesen, Nano Lett. **15**, 4616 (2015).
[20] B. Diaconescu, K. Pohl, L. Vattuone, L. Savio, P. Hofmann, V. M. Silkin, J. M. Pitarke, E. V. Chulkov, P. M. Echenique, D. Farias, and M. Rocca, Nature (London) **448**, 57 (2007).
[21] Y. Huang, S. N. Shirodkar, and B. I. Yakobson, J. Am. Chem. Soc. **139**, 17181 (2017).
[22] E. S. Penev, A. Kutana, and B. I. Yakobson, Nano Lett. **16**, 2522 (2016).
[23] L. Marušić and V. Despoja, Phys. Rev. B **95**, 201408 (2017).
[24] S. N. Shirodkar and E. Kaxiras, Phys. Rev. B **93**, 245438 (2016).
[25] Y. Guo, R. B. Smith, Z. Yu, D. K. Efetov, J. Wang, P. Kim, M. Z. Bazant, and L. E. Brus, J. Phys. Chem. Lett. **7**, 2151 (2016).
[26] K. Sugawara, K. Kanetani, T. Sato, and T. Takahashi, AIP Adv. **1**, 022103 (2011).
[27] S. Raza, G. Toscano, A.-P. Jauho, M. Wubs, and N. A. Mortensen, Phys. Rev. B **84**, 121412(R) (2011).
[28] J. J. Mortensen, L. B. Hansen, and K. W. Jacobsen, Phys. Rev. B **71**, 035109 (2005).
[29] J. Enkovaara, C. Rostgaard, J. J. Mortensen, J. Chen, M. Dułak, L. Ferrighi, J. Gavnholt, C. Glinsvad, V. Haikola, H. A. Hansen, H. H. Kristoffersen, M. Kuisma, A. H. Larsen, L. Lehtovaara, M. Ljungberg, O. Lopez-Acevedo, P. G. Moses, J. Ojanen, T. Olsen, V. Petzold, N. A. Romero, J. Stausholm-Møller, M. Strange, G. A. Tritsaris, M. Vanin, M. Walter, B. Hammer, H. Häkkinen, G. K. H. Madsen, R. M. Nieminen, J. K. Nørskov, M. Puska, T. T. Rantala, J. Schiøtz, K. S. Thygesen, and K. W. Jacobsen, J. Phys.: Condens. Matter **22**, 253202 (2010).
[30] P. E. Blöchl, Phys. Rev. B **50**, 17953 (1994).
[31] G. Kresse and D. Joubert, Phys. Rev. B **59**, 1758 (1999).
[32] J. Yan, J. J. Mortensen, K. W. Jacobsen, and K. S. Thygesen, Phys. Rev. B **83**, 245122 (2011).
[33] K. Andersen, K. W. Jacobsen, and K. S. Thygesen, Phys. Rev. B **86**, 245129 (2012).
[34] See Supplemental Material at http://link.aps.org/supplemental/10.1103/PhysRevB.97.195435 for a detailed discussion on transparent boundary conditions, calculation of carrier lifetimes, and figures for other modes.
[35] P. Narang, L. Zhao, S. Claybrook, and R. Sundararaman, Adv. Opt. Mater. **5**, 1600914 (2017).
[36] A. M. Brown, R. Sundararaman, P. Narang, W. A. Goddard, III, and H. A. Atwater, ACS Nano **10**, 957 (2016).
[37] A. M. Brown, R. Sundararaman, P. Narang, W. A. Goddard, and H. A. Atwater, Phys. Rev. B **94**, 075120 (2016).
[38] A. M. Brown, R. Sundararaman, P. Narang, A. M. Schwartzberg, W. A. Goddard, III, and H. A. Atwater, Phys. Rev. Lett. **118**, 087401 (2017).
[39] C. A. Rozzi, D. Varsano, A. Marini, E. K. U. Gross, and A. Rubio, Phys. Rev. B **73**, 205119 (2006).
[40] V. Despoja, D. Novko, K. Dekanić, M. Šunjić, and L. Marušić, Phys. Rev. B **87**, 075447 (2013).
[41] D. Guzman, H. Alyahyaei, and R. Jishi, 2D Mater. **1**, 021005 (2014).
[42] T. Low, F. Guinea, H. Yan, F. Xia, and P. Avouris, Phys. Rev. Lett. **112**, 116801 (2014).
[43] M. Jablan, H. Buljan, and M. Soljačić, Phys. Rev. B **80**, 245435 (2009).
[44] J. K. Jain and S. Das Sarma, Phys. Rev. B **36**, 5949 (1987).
[45] L. Yang, Nano Lett. **11**, 3844 (2011).
[46] G. Profeta, M. Calandra, and F. Mauri, Nat. Phys. **8**, 131 (2012).
[47] R. Roldán and L. Brey, Phys. Rev. B **88**, 115420 (2013).